

Mesoscopic Metal–Insulator Transition at Ferroelastic Domain Walls in VO₂

Alexander Tselev,^{†,*} Vincent Meunier,[†] Evgheni Strelcov,[‡] William A. Shelton, Jr.,[†] Igor A. Luk'yanchuk,[§] Keith Jones,^{||} Roger Proksch,^{||} Andrei Kolmakov,[‡] and Sergei V. Kalinin[†]

[†]Oak Ridge National Laboratory, Oak Ridge, Tennessee 37831, [‡]Physics Department, Southern Illinois State University, Carbondale, Illinois 62901, [§]University of Picardie Jules Verne, Amiens, 80039, France and L. D. Landau Institute for Theoretical Physics, Moscow, Russia, and ^{||}Asylum Research, Santa Barbara, California 93117

ABSTRACT The novel phenomena induced by symmetry breaking at homointerfaces between ferroic variants in ferroelectric and ferroelastic materials have attracted recently much attention. Using variable temperature scanning microwave microscopy, we demonstrate the mesoscopic strain-induced metal–insulator phase transitions in the vicinity of ferroelastic domain walls in the semiconductive VO₂ that nucleated at temperatures as much as 10–12 °C below bulk transition, resulting in the formation of conductive channels in the material. Density functional theory is used to rationalize the process low activation energy. This behavior, linked to the strain inhomogeneity inherent in ferroelastic materials, can strongly affect interpretation of phase-transition studies in VO₂ and similar materials with symmetry-lowering transitions, and can also be used to enable new generations of electronic devices through strain engineering of conductive and semiconductive regions.

KEYWORDS: vanadium dioxide · ferroelastic domains · domain walls · metal–insulator phase transition · near-field microwave microscopy · density functional theory

The electronic and structural properties of surfaces and interfaces in condensed matter is an area of intense fundamental and applied interest. It is well established that interfaces between two different materials can show a rich variety of properties different from the constituent materials as a result of electronic and atomic reconstructions induced by symmetry breaking.¹ Recent examples include interface mediated conduction,² superconductivity,³ magnetic effects,⁴ and improper ferroelectric responses.⁵ These phenomena are controlled by the interplay between misfit strains and charge transfer across the interfaces driven by the difference in chemical and polarization states, albeit recently more subtle effects related to the polarization⁶ and octahedra tilting and distortions have begun to be explored.^{7,8} However, the emergent physical behaviors at the heterointerfaces are typically driven by strain, charge transfer, and octahedral tilt couplings simultaneously, precluding the elucidation of the role of individual mechanisms.

The interfaces *within* homogeneous materials, namely boundaries between domains in ferroic materials, provide an ideal model system to explore the effect of symmetry breaking on materials behavior driven solely by the discontinuity of structural order parameters. Specifically, symmetry operations transforming one domain state of a ferroic material to another correspond to symmetry elements of the parent space group, which become lost upon structural transition.⁹ If a domain wall corresponds to a lost mirror plane of the higher-symmetry structure, this effectively raises the local symmetry, and atomic arrangement, interatomic bond lengths, and angles at the wall vicinity may resemble those of the parent structure, which leads to a local decrease of the phase-transition-driving order parameter and even a possible appearance of the parent phase properties at the domain wall at temperatures well below T_c . Furthermore, the discontinuity of the primary order parameter can generate secondary distortions in the vicinity of the wall, with examples including the deformation of oxygen octahedral in distorted perovskites and in-plane polarization components at domain walls in LiNbO₃.¹⁰ As a recent example, room temperature domain wall conductance in the insulating multiferroic BiFeO₃ was observed and attributed to the band gap reduction due to increased Fe–O–Fe angles.¹¹ Similarly, these walls are predicted to be magnetic.¹² This onset of conductance is possible despite the fact that the temperature transition to the corresponding higher-symmetry metallic phase is well above the room temperature. A surprising observation of superconductivity in twin walls of WO_{3-x} single crystals reported in ref 13 should be pointed out as well.

*Address correspondence to tseleva@ornl.gov.

Received for review March 3, 2010 and accepted July 14, 2010.

Published online July 21, 2010. 10.1021/nn1004364

© 2010 American Chemical Society

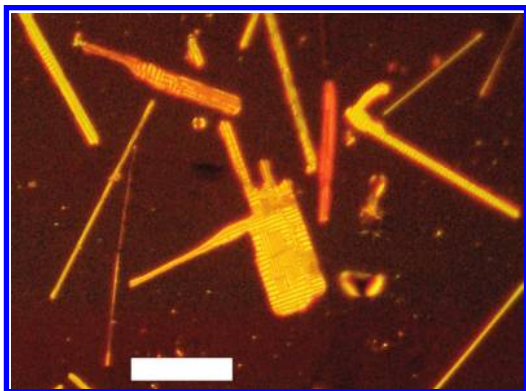


Figure 1. VO₂ nanoplatelets on a Si/SiO₂ substrate (optical image in polarized light). Scale bar is 50 μm.

However, in addition to the *intrinsic* symmetry breaking mechanisms, the emergent behavior in ferroic domain walls can be driven by the *extrinsic* factors related to the long-range electrostatic, chemical, or strain fields. Examples of these behaviors include the favorable segregation of oxygen vacancy in the vicinity of twin walls,¹⁴ screening at the ferroelectric walls, or aging in hard ferroelectric ceramics. While some of these mechanisms (*e.g.*, those associated with ionic diffusion) can be identified based on the kinetic studies, both phase transitions driven by electrostatic and strain fields will be rapid. Note that these behaviors, while being extrinsic to the physics of the walls *per se*, will still define the properties of any volume of material containing a significant amount of ferroic domains. Given that domains form in all situations of practical importance and single-domain states represent in general exceptions rather than a rule, the importance of these mesoscopic behaviors at ferroelastic interfaces cannot be exaggerated.

Here, we describe the formation of quasiperiodic homophase domain structures leading to parallel-plane organization of domain walls in the lower-symmetry phase of improper ferroelastic vanadium dioxide. Using scanning microwave microscopy (SMM), we systematically explore the metal–insulator transition in this system, and demonstrate the opening of conductive channels at ferroelastic domain walls at temperatures well below bulk transition. Density-functional theory is used to explore the intrinsic wall structure, and characterize the nucleation process of the metallic phase at the wall. The experiments were performed with strained as-grown single-crystalline VO₂ nanoplatelets on Si/SiO₂ substrates (Figure 1). On heating, vanadium dioxide undergoes a temperature-driven metal–insulator transition (MIT), and we observe that ferroelastic domain walls of a certain type in the lower-symmetry semiconducting phase serve as sites for nucleation of the higher-symmetry phase with dramatically larger electric conductivity. The localized, mesoscopic, phase transition along the domain walls results in about one micrometer wide metallic lines in the semiconducting matrix. The process of the metallic domain

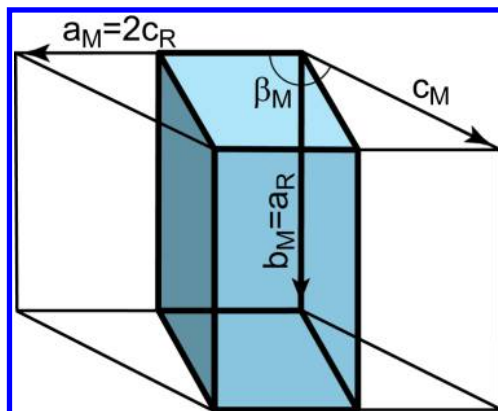


Figure 2. Relation between tetragonal (R phase) and monoclinic (M1 phase) unit cells. The tetragonal unit cell is shown with thicker lines. The difference in value of the angle b_M in M1 and R structures is about 0.6°.

formation has been imaged with the use of near-field SMM, which allows detection of local electrical conductance without the need for electrode fabrication to preserve the ferroelastic domain structure. *Ab initio* calculation of the electron spectrum showed band gap closure at a distance of about one unit cell from a domain wall in an unconstrained domain structure of this type, suggesting significant lowering of the local energy barrier for nucleation of the metallic phase.

RESULTS AND DISCUSSION

Domain Variants and Wall Structures in VO₂. In bulk, strongly correlated-electron oxide VO₂ undergoes a first order MIT at $T_c = 68$ °C with abrupt, about 5 orders of magnitude change in electrical conductivity. Owing to this transition, VO₂ previously attracted much attention from applied and fundamental perspectives.^{15–17} The lattice degrees of freedom take part in the phase transition, and the MIT is accompanied by a structural transformation making this material an improper ferroelastic. As a rule, large enough single-crystalline samples of the material are divided into ferroelastic domains (twinned) after cooling through the phase transition as a result of a reduction of lattice symmetry.^{18,19} The higher-symmetry metallic phase, R, has a tetragonal, rutile, crystal structure (space group $P4_2/mnm$, No. 136), whereas low-temperature and lower-symmetry semiconducting phase, M1, is monoclinic (space group $P2_1/c$, No. 14). The monoclinic distortion of the tetragonal phase upon transition from R to M1 occurs as a shear deformation along the tetragonal c -axis so that the monoclinic 2-fold axis b_{M1} is parallel to the a -axis of the tetragonal structure with the lattice basis transformation matrix $(002/100/01-1)$,²⁰ the unit cell becomes doubled along the tetragonal c -axis. Figure 2 illustrates the relationship between unit cells of R and M1 phases.

The space group of M1 phase is a maximal subgroup of the parent space group with index $i = 8$, and this structural transformation generates four pairs of orientational domain species in the lower-symmetry

phase, each pair corresponding to two equally oriented antiphase domains shifted in respect to each other by one tetragonal unit cell along the parent's structure c -axis. Four orientations of the domains correspond to four distinct directions of the monoclinic 2-fold axis b_{M1} along $\langle 100 \rangle_R$ directions of the parent lattice and can be visualized as consecutive rotations of one of the domains by 90° around the tetragonal c -axis. Regarding each pair of antiphase domains as one domain in the following (because domain physical properties along a definite direction in space are identical) we will call pairs of orientational domains as 90° and 180° domains according to the difference of the rotation angle between them around the tetragonal c -axis. Within the R-to-M1 transition, the lost symmetry planes and, consequently, possible domain walls of interest here are oriented along $\{010\}_R$ and $\{001\}_R$ crystallographic planes of the rutile structure for boundaries between 180° domains and $\{110\}_R$ planes for boundaries between 90° domains of the M1 phase. Importantly, domain boundaries corresponding to lost mirror planes of the parent phase point group automatically satisfy the mechanical compatibility condition,²¹ which requires equality of spontaneous strains in adjacent domains along the wall:

$$\mathbf{x}^T(\varepsilon_1 - \varepsilon_2)\mathbf{x} = 0 \quad (1)$$

where ε_1 and ε_2 are the spontaneous strain tensors and \mathbf{x} is a vector in the wall plane. Therefore, domain walls of this type are always permissible.

Experimental Observations. VO_2 nanoplatelets were grown using a vapor transport technique. As was verified by X-ray diffraction, the nanoplatelets are single-crystalline with the tetragonal c -axis parallel to the length and tetragonal $[110]_R$ direction normal to the substrate surface.²² The nanoplatelets thickness is close to 500 nm and is uniform along length. The length can be as large as a few hundred of micrometers with width being below a few micrometers. Because of the small size, the nanoplatelets are mechanically stable and remain unbroken even after multiple cycles of domain formation and disappearance in contrast to bulk single crystals, which are prone to cracking along domain walls upon transition to the low-temperature phase.¹⁹ At the same time, in comparison with sub-100 nm-small single-crystalline nanobeams,^{23–25} the micrometer-large width of the nanoplatelets allows application of a more versatile set of characterization techniques with a larger throughput to obtain information about many more aspects of the material behavior. Specifically, while 1D structures generally allow formation of domain walls perpendicular to the longitudinal axis, which thus can be completely strain-relaxed or under uniform strain, the 2D nature of the platelets generates multiple domain variants and hence geometric frustration between different domain orientations. At the

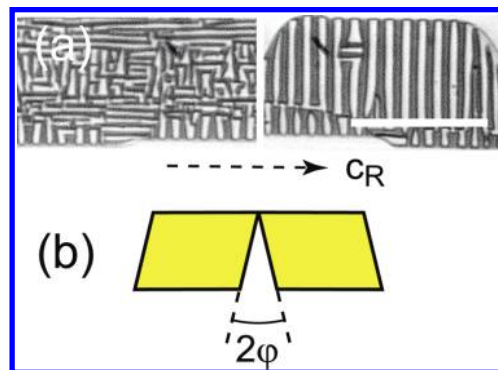


Figure 3. (a) Polarized light images of labyrinth and parallel-plane structures in the monoclinic phase, respectively. The scale bar is $10 \mu\text{m}$. (b) Definition of the clapping angle between two adjacent domains.

same time, in 2D systems domain structures can be easy to access for the local microscopic observations.

After high-temperature growth and cooling to room temperature, the nanoplatelets remain firmly attached to the substrate being under stress due differences in thermal expansion coefficients of VO_2 and substrate and change of the lattice parameters at MIT. The latter factor makes a significant contribution to the stress. At the structural transitions, the lattice contracts by about 1% along c_R and expand by about 0.6% along a_R and b_R .²⁶ The nanoplatelets are constrained to preserve their shape and lateral size and break into ferroelastic domains (twinned) to accommodate the change of the lattice geometry.

Inspecting samples under a polarized light microscope (monoclinic structure of M1 phase possesses biaxial birefringence), three primary ferroelastic domain patterns were identified at room temperature: (a) a labyrinth structure, consisting mostly of 90° domains (Figure 3a, left), (b) a lamellar structure with 90° domains and domain walls running along the nanoplatelets length (not shown), and (c) a parallel-plane 180° domain structure with walls across nanoplatelets perpendicular to the nanoplatelets length (Figure 3a, right). Formation of a specific structure is determined by geometry of a particular nanoplatelet and strength of its interaction with the substrate.

For known crystallographic orientation of the single-crystalline nanoplatelets, the types of domain walls in each nanoplatelet can be identified. In the M1 structure, there are three types of walls satisfying the mechanical compatibility conditions eq 1. Namely, permissible walls can be oriented along $\{010\}_R$, $\{001\}_R$, $\{110\}_R$, and approximately along $\{112\}_R$ planes of the unconstrained parent structure. Analysis of the polarized light photographs reveals that only walls of the last three types really appear in the nanoplatelets attached to substrates. We will denote these walls $W_{\{001\}_R}$, $W_{\{110\}_R}$, and S , respectively. All walls parallel to the nanoplatelet length are of $W_{\{110\}_R}$ type and separate 90° domains. $W_{\{001\}_R}$ walls are oriented perpendicular to the nanoplatelet length

and separate 180° domains. Under conditions of no constraints, *S*-type walls separating 90° domains make an angle of about 24° with the direction normal to the nanoplatelets length. However, under stress, these walls can rotate and be oriented perpendicular to the nanoplatelet length. (*S*-type walls satisfy eq 1 by running along general crystallographic planes $\{hkl\}$ with h , k , and l being dependent on the values of lattice constant in a particular structure; therefore, their position depends on the lattice parameters and strain.)

As illustrated in the inset in Figure 3b, domains separated by a $W_{\{001\}}$ wall should be rotated toward each other in order to maintain material integrity. The required rotation angle, called clapping angle (or twin obliqueness), can be calculated from simple geometrical considerations, and $\varphi \approx 0.32^\circ$ in unconstrained samples in this case. For comparison, the clapping angle associated with $W_{\{110\}}$ walls is about 0.05° (since spontaneous strain deforms the basal planes of the rutile cell from squares to rectangles). It can be shown that *S*-type walls maintain material integrity with a clapping angle $\varphi \approx 0$.

The large difference between clapping angles associated with 180° $W_{\{001\}}$ walls and with *S*-type walls makes it possible to distinguish between them by imaging topography over the domain structure. The signature of the 180° domain structure in topographic AMF images is quasi-periodically alternating ridges and furrows appearing due to a fairly large clapping angle specific for the $W_{\{001\}}$ walls. These features are clearly visible in the topographic AFM images. Polarized light images of the 180° structures reveal quasi-periodic sequences of dark and bright stripes running across all nanoplatelet width as shown in Figure 3a, right. Taking into account the nanoplatelets crystallographic orientation, the value of the clapping angle when being measured along the nanoplatelets surface is 0.23° . From topographic AFM images, this value in our samples is in the range 0.2° – 0.3° , which is close to the calculated value.

Variable-Temperature Microwave Imaging of Domain Wall

Conductance. The local conductivity over domain structures was imaged using scanning near-field microwave microscopy as a function of temperature. Figure 4 shows a schematic of the SMM probe configuration. The SMM is sensitive to local contrast in conductance, and allows for clear contrast between metallic and insulating regions with ~ 100 nm resolution. The advantage of this method is that the imaging does not require fabrication of metallic electrodes, and also allows one to visualize insulating regions of metallic phase. As we noticed, electrodes deposited over the nanoplatelets tend to disturb the domain structure and turn the domain walls along their edges (possibly, due to residual elastic stress in metallic film of the electrodes) preventing imaging of the domain wall conductance at dc. Furthermore, the metallic domain ensconced in

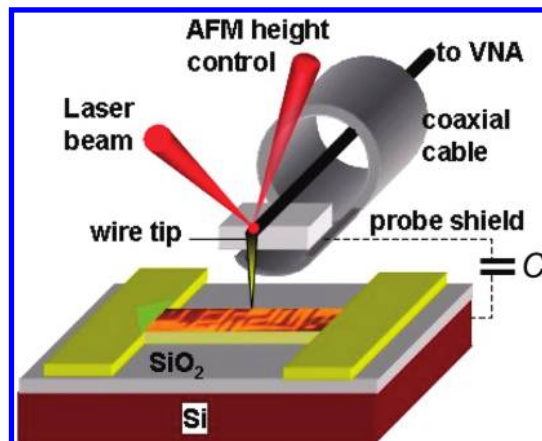


Figure 4. Schematic of the SMM setup (probe part). C is the stray capacitance between substrate and the probe shield (outer conductor of the coaxial cable).

the insulating matrix will not be visible in any dc-current-based conductive imaging mode.

The MIT is of the first order, and in strained flakes on a substrate, the transition takes place over a broad temperature intervals, which is from about 55 to 140°C in our case. During the phase transition, the nanoplatelets are split along length into heterophase domains spanning the whole width. The domains are self-organized into quasi-periodic structures, minimizing the elastic energy of the nanoplatelet–substrate system, similar to the behavior observed in nanobeams.²⁷

Figure 5 shows AFM topography and SMM images of the early stage of the semiconductor-to-metal transition over a structure of the 180° domains. The image at 50°C was taken a few degrees Celsius before the beginning of the transition on heating. One metallic domain elongated along ridges on the surface is clearly visible in the upper right corner of the next SMM image taken at 57°C . Three elongated metallic domains are visible within the scan frame at $T = 61^\circ\text{C}$. The scan of next pair of images starts at the same temperature. The direction of the slow scan is shown with an arrow. At the scan line indicated by the dashed line, temperature was increased by about 2°C , and a number of new metallic domains appeared. Note that metallic domains nucleate at the ridges and grow into furrows of the corrugated topographic structure. The ridges corresponding to metallic domains look slightly elevated above the surface. This is due to expansion of the lattice by about 0.6% in the direction normal to the surface as a result of the structural transition. After transition is complete, the surface is randomly rough (the rightmost topography image, upper part), and on cooling, the structure reappears in reverse order so that the metallic domains disappear in the ridges. We note, that similar experiments over 90° walls showed that walls of this type do not serve as preferential sites for nucleation of the metallic phase and do not show a distinct behavior in the phase transition.

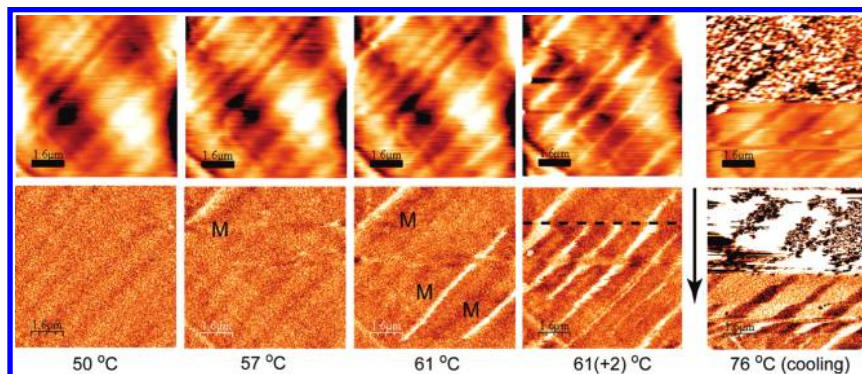


Figure 5. AFM topography images (upper row) and corresponding amplitude signal SMM images (lower row) acquired simultaneously over a 180° domain structure. Except the rightmost column, the images were acquired at the initial stage of the MIT at different temperatures on heating. The images of the rightmost column were acquired while changing temperature on cooling. Darker color corresponds to lower height in topography and lower conductance in SMM images. M labels metallic domains (not all domains are labeled). The arrow indicates the scan direction. The horizontal dashed line in the $61(+2)^\circ\text{C}$ SMM image indicates the scan line where temperature was increased by about 2°C during scanning. The sample temperature was 61°C at the beginning of the scan. The rightmost pair of images was acquired between 76 and 60°C on cooling from the metallic phase. The SMM image was flattened to (dramatically) reduce the contrast between signals from sample in the metallic state (upper part) and in the multidomain state (lower part). Scale bars are $1.6\ \mu\text{m}$.

The following scenario of 180° domain pattern formation emerges from this observation. On cooling from the homogeneous metallic state, semiconducting domains nucleate and become self-organized into a quasi-periodic structure along the nanoplatelet length. On further cooling, metallic domains shrink in size keeping the quasi-periodic one-dimensional structure along the nanoplatelet length. To ensure lattice coherence at the heterophase domain boundaries, the lattice of the monoclinic phase turns to be under tensile stress along normal to the nanoplatelet surface because its lattice constant is smaller in this direction. It defines the direction of the shear distortion in the monoclinic phase so that ridges are formed at the locations where metallic domains disappear at the end of the transition. At low temperatures, the material is more under compression at the ridges than at furrows. This compression is along the c_R -axis, and since the R phase has a shorter lattice constant along c_R , upon warming, the compression promotes nucleation of metallic domains at ridges, but not furrows with the transformation process proceeding in the reversed way. As follows from this scenario, a large contrast in domain clapping angles and, consequently, associated elastic stress between domain walls of different types makes the 180° walls corresponding to the ridges behave differently from all other walls in the course of the phase transition.

Since only two homophase domain types out of four possible are present after transition is complete in the resulting structure, this configuration of ferroelastic domains is unstable and may undergo reconstruction to minimize the overall energy of the flake or may remain metastable like in the described case. We note that since the clapping angle is negligibly small for S -type walls, they are more energeti-

cally favorable than 180° walls because of a smaller elastic stress associate with them. This makes 180° wall structures prone to reconstruction into labyrinth patterns of 90° domains, as was in fact observed in our samples after multiple cycling between semiconducting and metallic states. However, the structure is stable in respect to temperature changes in a range within the phase transition interval.

Electronic Structure of the Ferroelastic Domain Walls in VO_2 .

The experimental observations illustrate that the ferroelastic domain walls in VO_2 are associated with the formation of the metallic phase channel to reduce the long-range strain fields. This formation of conductive domains seems to automatically follow the atomic displacements in the ferroelastic wall structure, suggesting low intrinsic activation energy for formation of the metallic phase. Qualitatively, this behavior can be rationalized from a simple Ginzburg–Landau theory for a first-order phase transition.

Let us analyze the behavior of the order parameter across a 180° wall. According to the results of Brews,¹⁹ the transition is described by a four-component order parameter (OP) $\vec{\eta} = (f_1, f_2, f_3, f_4)$. Its normalized value for a representative domain of the M1 phase is $\vec{\eta}_{M1}^0 = (1/\sqrt{2})(\varepsilon, \varepsilon, 0, 0)$. The OP value of the domain rotated by 180° around c_R is $\vec{\eta}_{M1}^{180} = (1/\sqrt{2})(\varepsilon, -\varepsilon, 0, 0)$, and the two 90° domains correspond to $\vec{\eta}_{M1}^{\pm 90} = (1/\sqrt{2})(0, 0, \varepsilon, \pm\varepsilon)$. When both $f_{1,2}$ or $f_{3,4}$ change sign, it corresponds to antiphase domains with the same orientation. Change of the OP across a domain wall can be imaged as a rotation of a vector with variable length in the four-dimensional space of the OP.²⁸ The metallic phase at the wall appears if all f_i are equal to zero within the wall. For the 180° wall, f_2 goes through zero (because it changes

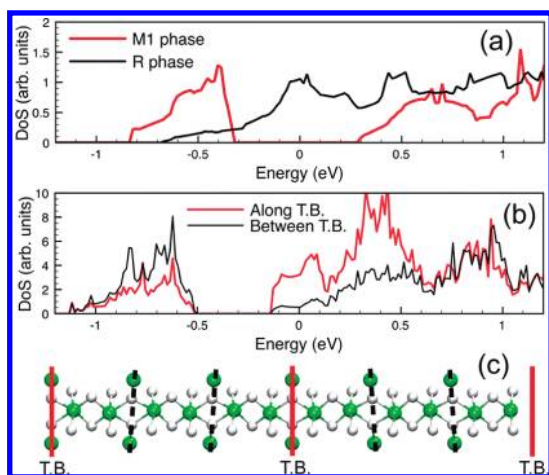


Figure 6. (a) Density of states (DOS) in bulk semiconducting M1 and metallic R phases of VO_2 ; (b) averaged DOS at vanadium atoms along twin boundaries (T.B.) and between twin boundaries; (c) schematic of the model structure used for DFT calculations.

sign), while f_1 may remain constant or go to zero too, returning back to the original value on the opposite side of the wall. The first scenario corresponds to the appearance of the M2 phase,²⁹ which has a spontaneous strain with shear component normal to c_R , $S_{xz} \neq 0$ (z axis is equivalent to c_R) as well as $(S_{xx} - S_{yy}) \neq 0$,¹⁹ whereas the second case implies existence of the metallic-phase structure with zero spontaneous strain. Taking this into account, the formation of the M2 phase is associated with excess elastic energy and therefore less favorable. Similar analysis for the 90° walls cannot be done because 90° domains are represented by different pairs of order parameter components with less defined possibilities of OP behavior.

To further clarify whether the electronic structure at a 180° domain wall can be responsible for the observed nucleation of the metallic domains exclusively at this type of domain walls, we performed *ab initio* calculations of the electronic spectrum in the vicinity of the 180° domain walls. The calculated density of states of both M1 and R systems in bulk is shown in Figure 6a. The M1 phase is found to be 101 meV more stable per VO_2 unit, compared to the R phase, in agreement with experimental observation. A number of twinned structures were constructed by repeating the relaxed M1 structure obtained from the simulations along the $[001]_R$ direction. The twin structure was built by aligning one row of V atoms normal to $[001]_{R_1}$ and using this row as a mirror plane to generate the second half of the cell. To make the cell periodic a second twin is introduced, the twin unit cell is shown schematically in Figure 6c. Similar structures with varying distance between twin boundaries were generated using the above scheme. In each case a $2 \times 4 \times 4$ Monkhorst–Pack grid was used to ensure conver-

gence. The “twin energy” was obtained by subtracting the total energy of the structure from the corresponding energy of the M1 crystal structure. The resulting energy was divided by two in order to get an energy per twin boundary. We found that the energy for twinning quickly converges to ~ 250 meV per twin as a function of increasing distance between twin boundaries, indicating that the interface energy is well localized at the boundary. The electronic property of the 3.3 nm long unit cell is shown in Figure 6b. The local density of states was obtained using the tetrahedron method (96 tetrahedrons were used). The plot of the density of states indicates that a metallic character develops right on the twin boundary and quickly dies off as we move away from the boundary. We have found also that electronic properties vary along the twin boundary depending on the local environment and on the tilt angle of the neighboring cells relative to the boundary.

As is seen, the calculations clearly indicate that the 180° domain boundary is already in a configuration close to that of metallic phase, and therefore the nucleation barrier for the higher-symmetry metallic phase can be expected to be sufficiently reduced in comparison with the surrounding material. Moreover, the domain wall may possess metallic conductance at temperatures well below the MIT.

SUMMARY AND PERSPECTIVES

The domain structures and ferroelastic domain walls in semiconducting VO_2 are systematically analyzed, and the dominant domain populations in nanoplatelets are identified. Using microwave microscopy, we observe the mesoscopic-strain-driven metal–insulator transition at ferroelastic domain walls in VO_2 that occurs at temperatures well below corresponding bulk transition. The density functional theory studies suggest that the twin walls contain atomically thick conductive channels with metallic properties. While not observed directly here, this region with high-temperature phase properties acts as an effective nucleus for the formation of the mesoscopic strain-driven phase, explaining coexistence and evolution of metallic phases at ferroelastic walls.

The implications of these studies are 2-fold. The formation of twins in macro- and mesoscopic volumes of ferroic materials is a rule rather than exception, and is directly involved in, for example, shape-memory, superelasticity, and other functionalities. Furthermore, ferroelastic domain patterns adjust to accommodate the macroscopic or microscopic (*e.g.*, due to grain structure or any heterogeneity) strains. Even in the strain-free cases, the symmetry breaking at the phase transition will give rise to (frustrated) domain patterns. Correspondingly, transition from the insulating low-symmetry to metallic high-symmetry phases as a route

for strain accommodation (as opposed to the formation of progressively smaller domain patterns as in morphotropic systems and martensites) will significantly affect the physics of this material, and calls for re-examination of the results of studies of metal–insulator phase transition in these systems. The mixed metal–insulator states driven by strain inhomogeneity and reminiscent of a relaxor state in disordered ferroelectrics can possess many unusual dielectric behaviors intrinsic to nanocomposite materials. These fundamental observations will help to understand the nature of hysteretic phenomena and improve the performance of in VO₂ nanodevices.³⁰

Second, these results illustrate that strain control of materials with symmetry-breaking metal–insulator

transition can be readily used to enable new classes of electronic and electro-optic devices configurable through extrinsic strains. In the example here, the strains at the domain walls generated well-oriented mesoscopic conductive channels that opened and closed in response to ferroelastic domain structure channels and can be tuned by temperature. Correspondingly, combining these systems with the strain control (e.g., using ferroelectric substrates) can allow direct fabrication of tunable electronic devices. Perhaps even more excitingly, the strain-dependent transport properties of VO₂ and bias-dependent strains in ferroelectrics can be synergistically combined to enable adaptive and reconfigurable logic devices utilizing both electronic and strain degrees of freedom.

EXPERIMENTAL AND THEORETICAL METHODS

VO₂ nanoplatelets were grown with a vapor transport technique on SiO₂/Si or quartz substrates at ca. 1000 °C using VO₂ fine powder (Alfa-Aesar 99%) as a precursor and argon as a carrier gas (13 Torr, 3 sccm flow rate) following the procedure of ref 22. Since VO₂ has rather low vapor pressure at this temperature, vanadium pentoxide impurity serves as a precursor for nucleation and growth of the V_xO_y nanostructures. The latter become reduced to VO₂ upon further heating in oxygen-free atmosphere. The domain structure in VO₂ nanostructures was characterized both in transmission and in reflection modes using a Nikon L150 optical microscope.

Scanning microwave microscopy is realized on Asylum Research MFP-3D atomic force microscope platform. A Pt solid wire AFM cantilever tip (Rocky Mountain Nanotechnology) is connected to a coaxial cable (transmission line) through an impedance-matching network and then to a vector network analyzer (VNA) (Agilent E5062A). Contact mode AFM topography image and the SMM image are acquired simultaneously. Amplitude and phase of the microwave signal reflected from the tip (S11) are measured with the VNA while scanning over the sample surface in contact AFM mode. The complex value of the reflection coefficient S11 is determined by the capacitance of the system tip–substrate–outer conductor of the coaxial cable. Specifically for these experiments, as is clear from the scheme in Figure 4, a capacitance between a metallic area of a nanoplatelets and the Si substrate is in the series with substrate–cable outer conductor stray capacitance. At the imaging frequency of 1.78 GHz, the former capacitance is sufficiently large to allow flow of a large enough displacement current through the nanoplatelet portion right under the tip apex and to measurably alter the reflection coefficient of the tip–substrate system when the MIT takes place. Temperature control of a sample during imaging was achieved via Joule heating of the Si substrate by a DC current running through it. Sample temperature was measured by a miniature thermocouple directly attached to the substrate with a drop of a silver paint.

Density functional theory calculations were performed using the Vienna *ab initio* simulation package (VASP). The local density approximation (LDA) is known to fail for describing bulk VO₂ systems, where LDA predicts a metallic tetragonal (R) phase instead of the monoclinic (M1) phase at zero temperature. In fact, LDA predicts the M1 phase to be metallic rather than insulating. This is due to the presence of localized (strongly correlated) *d* electrons from vanadium. This can be remedied, at least qualitatively, by introducing a strong intra-atomic interaction (*U*) in a screened Hartree–Fock-like manner, as an on site correction to LDA. This approach is known as the LDA+*U* method. Here, we used the simplified, rotationally invariant, approach of Dudarev *et al.*³¹ with *U* = 4.0 and *J* = 0.78 eV. The Kohn–Sham equations were solved using the projector augmented wave (PAW) approach and a plane-wave basis with a 500 eV energy cutoff and

0.01 eV Gaussian broadening. All the results presented here were obtained using the 3s²3p⁶3d³4s² and 2s²2p⁴ valence configurations for vanadium and oxygen, respectively. Bulk properties of VO₂ (atom positions and lattice) were relaxed using a 6 × 6 × 12 (R) and 6 × 6 × 6 (M1) Monkhorst–Pack Brillouin zone sampling, resulting in a crystal structure with *a* = *b* = 0.455 nm and *c* = 0.277 nm (for R structure) and *a* = 0.553 nm, *b* = 0.455 nm, *c* = 0.534 nm, β = 121.6° (for M1 structure). The experimental lattice parameters are *a* = *b* = 0.456 nm; *c* = 0.300 nm (R), and *a* = 0.574 nm, *b* = 0.452 nm, *c* = 0.538 nm, β = 122.61° (M1). The calculated lattice parameters and volumes are in excellent agreement with experimental values.

Acknowledgment. Authors are grateful to Alexander Tagantsev for helpful discussions. Research at Oak Ridge National Laboratory's Center for Nanophase Materials Sciences was sponsored by the Scientific User Facilities Division, Office of Basic Energy Sciences, U.S. Department of Energy. The work of I.L. was supported by ANR project LOMACOQU. The research at SIUC was supported through NSF ECCS-0925837 and SISGR-DOE ERKCM67.

REFERENCES AND NOTES

- Okamoto, S.; Millis, A. J. Electronic Reconstruction at an Interface between a Mott Insulator and a Band Insulator. *Nature* **2004**, *428*, 630–633.
- Ohtomo, A.; Hwang, H. Y. A High-Mobility Electron Gas at the LaAlO₃/SrTiO₃ Heterointerface. *Nature* **2004**, *427*, 423–426.
- Reyren, N.; Thiel, S.; Caviglia, A. D.; Kourkoutis, L. F.; Hammer, G.; Richter, C.; Schneider, C. W.; Kopp, T.; Ruetschi, A. S.; Jaccard, D. Superconducting Interfaces between Insulating Oxides. *Science* **2007**, *317*, 1196–1199.
- Brinkman, A.; Huijben, M.; van Zalk, M.; Huijben, J.; Zeitler, U.; Maan, J. C.; van der Wiel, W. G.; Rijnders, G.; Blank, D. H. A.; Hilgenkamp, H. Magnetic Effects at the Interface between Nonmagnetic Oxides. *Nat. Mater.* **2007**, *6*, 493–496.
- Bousquet, E.; Dawber, M.; Stucki, N.; Lichtensteiger, C.; Hermet, P.; Gariglio, S.; Triscone, J.-M.; Ghosez, P. Improper Ferroelectricity in Perovskite Oxide Artificial Superlattices. *Nature* **2008**, *452*, 732–736.
- Tagantsev, A. K.; Gerra, G.; Setter, N. Short-Range and Long-Range Contributions to the Size Effect in Metal–Ferroelectric–Metal Heterostructures. *Phys. Rev. B* **2008**, *77*, 174111-1–174111-9.
- May, S. J.; Kim, J.-W.; Rondinelli, J. M.; Karapetrova, E.; Spaldin, N. A.; Bhattacharya, A.; Ryan, P. J. Quantifying Octahedral Rotations in Strained Perovskite Oxide Films. *Mater. Sci., Condens. Matter*, published online February 5, 2010; <http://arxiv.org/abs/1002.1317v1>.

8. Borisevich, A.; Chang, H. J.; Huijben, M.; Oxley, M. P.; Okamoto, S.; Niranjana, M. K.; Burton, J. D.; Tsybmal, E. Y.; Chu, Y. H.; Yu, P. et al. Suppression of Octahedral Tilts and Associated Changes of Electronic Properties at Epitaxial Oxide Heterostructure Interfaces. *Mater. Sci., Condens. Matter*, published online February 16, 2010; <http://arxiv.org/abs/1002.2989>.
9. Wadhawan, V. K. *Introduction to Ferroic Materials*; Gordon & Breach: Amsterdam, The Netherlands, 2000.
10. Morozovska, A. N.; Eliseev, E. A.; Li, Y.; Svechnikov, S. V.; Maksymovych, P.; Shur, V. Y.; Gopalan, V.; Chen, L.-Q.; Kalinin, S. V. Thermodynamics of Nanodomain Formation and Breakdown in Scanning Probe Microscopy: Landau–Ginzburg–Devonshire Approach. *Phys. Rev. B* **2009**, *80*, 214110-1–214110-12.
11. Seidel, J.; Martin, L. W.; He, Q.; Zhan, Q.; Chu, Y. H.; Rother, A.; Hawkridge, M. E.; Maksymovych, P.; Yu, P.; Gajek, M. Conduction at Domain Walls in Oxide Multiferroics. *Nat. Mater.* **2009**, *8*, 229–234.
12. Catalan, G.; Scott, J. F. Physics and Applications of Bismuth Ferrite. *Adv. Mater.* **2009**, *21*, 2463–2485.
13. Aird, A.; Salje, E. K. H. Sheet Superconductivity in Twin Walls: Experimental Evidence of WO_{3-x} . *J. Phys.: Condens. Matter* **1998**, *10*, L377–L380.
14. Goncalves-Ferreira, L.; Redfern, S. A. T.; Artacho, E.; Salje, E.; Lee, W. T. Trapping of Oxygen Vacancies in the Twin Walls of Perovskite. *Phys. Rev. B* **2010**, *81*, 024109-1–024109-7.
15. Zylbersztein, A.; Mott, N. F. Metal-Insulator Transition in Vanadium Dioxide. *Phys. Rev. B* **1975**, *11*, 4383–4395.
16. Qazilbash, M. M.; Brehm, M.; Chae, B.-G.; Ho, P. C.; Andreev, G. O.; Kim, B.-J.; Yun, S. J.; Balatsky, A. V.; Maple, M. B.; Keilmann, F. Mott Transition in VO_2 Revealed by Infrared Spectroscopy and Nano-Imaging. *Science* **2007**, *318*, 1750–1753.
17. Booth, J. M.; Casey, P. S. Anisotropic Structure Deformation in the VO_2 Metal–Insulator Transition. *Phys. Rev. Lett.* **2009**, *103*, 086402-1–086402-4.
18. Fillingham, P. J. Domain Structure and Twinning in Crystals of Vanadium Dioxide. *J. Appl. Phys.* **1967**, *38*, 4823–4829.
19. Brews, J. R. Symmetry Considerations and the Vanadium Dioxide Phase Transition. *Phys. Rev. B* **1970**, *1*, 2557–2568.
20. Marezio, M.; McWhan, D. B.; Remeika, J. P.; Dernier, P. D. Structural Aspects of the Metal–Insulator Transitions in Cr-Doped VO_2 . *Phys. Rev. B* **1972**, *5*, 2541–2551.
21. Sapriel, J. Domain-Wall Orientations in Ferroelastics. *Phys. Rev. B* **1975**, *12*, 5128–5140.
22. Guiton, B. S.; Gu, Q.; Prieto, A. L.; Gudiksen, M. S.; Park, H. Single-Crystalline Vanadium Dioxide Nanowires with Rectangular Cross Sections. *J. Am. Chem. Soc.* **2005**, *127*, 498–499.
23. Wei, J.; Wang, Z.; Chen, W.; Cobden, D. H. New Aspects of the Metal–Insulator Transition in Single-Domain Vanadium Dioxide Nanobeams. *Nat. Nanotechnol.* **2009**, *4*, 420–424.
24. Zhang, S.; Chou, J. Y.; Lauhon, L. J. Direct Correlation of Structural Domain Formation with the Metal–Insulator Transition in a VO_2 Nanobeam. *Nano Lett.* **2009**, *9*, 4527–4532.
25. Sohn, J. I.; Joo, H. J.; Ahn, D.; Lee, H. H.; Porter, A. E.; Kim, K.; Kang, D. J.; Welland, M. E. Surface-Stress-Induced Mott Transition and Nature of Associated Spatial Phase Transition in Single Crystalline VO_2 Nanowires. *Nano Lett.* **2009**, *9*, 3392–3397.
26. Kucharczyk, D.; Niklewski, T. Accurate X-Ray Determination of the Lattice Parameters and the Thermal Expansion Coefficients of VO_2 near the Transition Temperature. *J. Appl. Crystallogr.* **1979**, *12*, 370–373.
27. Wu, J.; Gu, Q.; Guiton, B. S.; de Leon, N. P.; Ouyang, L.; Park, H. Strain-Induced Self-Organization of Metal–Insulator Domains in Single-Crystalline VO_2 Nanobeams. *Nano Lett.* **2006**, *6*, 2313–2317.
28. Sidorkin, A. S. *Domain Structure in Ferroelectrics and Related Materials*; Cambridge International Science Publishing: Cambridge, UK, 2006.
29. Paquet, D.; Leroux-Hugon, P. Electron Correlations and Electron-Lattice Interactions in the Metal-Insulator, Ferroelastic Transition in VO_2 : A Thermodynamical Study. *Phys. Rev. B* **1980**, *22*, 5284–5301.
30. Strelcov, E.; Lilach, Y.; Kolmakov, A. Gas Sensor Based on Metal–Insulator Transition in VO_2 Nanowire Thermistor. *Nano Lett.* **2009**, *9*, 2322–2326.
31. Dudarev, S. L.; Botton, G. A.; Savrasov, S. Y.; Humphreys, C. J.; Sutton, A. P. Electron-Energy-Loss Spectra and the Structural Stability of Nickel Oxide: An LSDA+U Study. *Phys. Rev. B* **1998**, *57*, 1505–1509.